Journal of Environmental Chemical Engineering 13 (2025) 116777

Contents lists available at ScienceDirect

Journal of Environmental Chemical Engineering

journal homepage: www.elsevier.com/locate/jece

Enhanced photocatalytic efficiency of a novel GO/Bi_2SO_5/AgBr ternary heterojunction for the degradation of tetracycline and rhodamine B

Adewumi O. Oluwole [a], Tunde L. Yusuf [b], Shepherd M. Tichapondwa [a], Michael O. Daramola [a], Samuel A. Iwarere [a,*]

[a] Department of Chemical Engineering, Faculty of Engineering, Built Environment and Information Technology, University of Pretoria, Hatfield, Pretoria 0002, South Africa

[b] Department of Chemistry, Faculty of Natural and Agricultural Sciences, University of Pretoria, Hatfield, Pretoria 0002, South Africa

ARTICLE INFO

Keywords:
Ternary composite
Tetracycline
Rhodamine B
Visible light irradiation
Photodegradation

ABSTRACT

Water contamination by pharmaceuticals and organic dyes requires advanced photocatalysts to degrade these pollutants effectively. This study used an in-situ precipitation method to synthesize a novel GO/Bi_2SiO_5/AgBr heterojunction photocatalyst and thoroughly analysed it for its structure, optical properties, and photocatalytic performance. Characterization techniques confirmed the successful integration of GO, Bi_2SiO_5, and AgBr, with BET analysis showing a significant surface area increase from 20.50 m^2/g to 47.44 m^2/g. Incorporating GO and AgBr extended visible-light absorption and improved charge separation, as demonstrated by UV-Vis DRS, PL spectra, EIS, and Mott-Schottky measurements. As a result, the photocatalyst achieved high degradation efficiencies of 95.83 % for tetracycline in 60 min and 97.02 % for Rhodamine B in 30 min under visible light. This improvement is attributed to the surface plasmon resonance (SPR) effect of Ag in AgBr and the electron-accepting ability of GO, which enhances charge transfer. Additionally, the photocatalyst showed excellent stability and reusability over five cycles. Quenching experiments confirmed that h^+ and $\bullet O_2^-$ radicals were key in pollutant degradation. This study provides a promising strategy for designing efficient, visible-light-driven photocatalysts for sustainable water treatment.

1. Introduction

The shortage and the continuous depletion of water resources across the globe as a result of population growth and the production of various dangerous organic contaminants such as pharmaceuticals, personal care products, pesticides, polyaromatic compounds, and dyes in wastewater underscore the urgent need for efficient and effective wastewater treatment methods [1–3]. Among the various organic contaminants, tetracycline (TCN) ranks among the mainly employed antibiotics globally, owing to their extensive application in clinical treatment, animal husbandry, and aquaculture [4,5]. They are also acknowledged for their economical nature and strong bactericidal capabilities [6–8]. Due to their toxic nature, organic dyes such as rhodamine (RhB) are one of the major contaminants of industrial wastewater from the textile industry, provoking adverse health problems in humans [9,10]. The presence of these contaminants in aqueous matrices has been shown to remain in the water and soil for extended periods, causing severe health risks to living organisms, reducing soil fertility and the photosynthetic activity of aquatic plants, hence impacting the development of anoxic conditions for marine fauna and flora within the ecosystem [11–14].

Consequently, the efficient removal and degradation mechanism of these contaminants, such as TCN and RhB in aqueous matrices, has been identified as a significant scientific issue that needs urgent solutions. Various water treatment techniques such as material adsorption, membrane filtration, chemical oxidation, biosurfactant method, and activated sludge process have proven inadequate in degrading them [15–18]. Recently, photocatalytic techniques for the degradation of TCN and RhB have received attention as they enable the oxidative degradation of organic pollutants in wastewater to produce CO_2 and H_2O at room temperature [19,20]. As a member of the Aurivillius family, Bi_2SiO_5 semiconductors possess promising potential for degrading organic contaminants in wastewater due to their appealing electronic and structural properties [21,22]. This is due to the migration of photo-induced charge carriers within the Bi_2SiO_5 semiconductor, which is attributed to the composition layered structure of the $[Bi_2O_2]^{2+}$ layers and $[SiO_3]^{2-}$ pyroxene file slabs [23,24]. However, this single

* Corresponding author.
E-mail address: samuel.iwarere@up.ac.za (S.A. Iwarere).

https://doi.org/10.1016/j.jece.2025.116777
Received 14 January 2025; Received in revised form 3 April 2025; Accepted 24 April 2025
Available online 24 April 2025

semiconductor has a wide bandgap of 3.54 eV, low specific surface areas, and easy recombination of photogenerated electrons and holes, which limit its photocatalytic efficiency for the degradation of organic contaminants under visible light irradiation [25].

The synthesis of heterojunction photocatalysts has proven to be a valuable technique for overcoming these limitations. Therefore, many heterojunction photocatalysts such as BiOBr/Bi_2SiO_5 [26], TiO_2/Bi_2SiO_5 [21], Bi_2SiO_5/g-C_3N_4 [27], and Bi_2SiO_5/$BiPO_4$ [28] have been synthesized and reported. The synthesized heterojunction photocatalysts show that heterojunction formation with Bi_2SiO_5 semiconductor possesses a superior photocatalytic activity in visible light degradation of the selected organic pollutants compared to pristine Bi_2SiO_5 photocatalysts. The exceptional photocatalytic efficiency of the synthesized Bi_2SiO_5 heterojunction photocatalyst can be attributed to the well-aligned straddling bandgap structures, which can promote the flow of charge carriers via the heterojunction, extended light absorbance, and a large specific surface area [22]. Despite this, it is still essential to filter suitable heterojunction components for Bi_2SiO_5 that can effectively promote the flow of charge carriers via the heterojunction interfaces and expand the light response range of the photocatalytic system for improved photocatalytic efficiency in the degradation of organic pollutants under visible light irradiation. On the other hand, AgBr has been recognized as a promising visible-light-triggered plasmonic photocatalyst due to its excellent photosensitivity, hence enhancing the visible light absorption of the photocatalysts through the surface plasmon resonance (SPR) of the Ag nanoparticles [29].

The formation of heterojunctions is theoretically possible since the band positions of Bi_2SiO_5 (3.54 eV) and AgBr (2.63 eV) are matched [30]. Hence, the importance of ensuring the smooth photo-charge carrier migration between the neighboring photocatalyst in the binary Bi_2SiO_5/AgBr heterojunction system is of paramount significance to warrant improved photocatalytic activity with the incorporation of GO into the heterojunction composites owing to the beneficial effect of GO as an electron shuttle for photo-charge carrier migration across the heterostructure interface and thus alleviating the current issues within the binary heterostructure system [31,32]. Despite various studies on the photocatalytic activity of Bi_2SiO_5 with other semiconductors, a systematic study on the effects of GO nanosheets as an electron sink and Ag nanoparticle as a plasmonic factor to boost the photocatalytic activity of Bi_2SiO_5 for the degradation of pollutants like tetracycline and rhodamine B under visible light illumination has not yet been reported.

Therefore, in this study, GO and AgBr were anchored onto Bi_2SiO_5 by a facile in situ co-precipitation method to provide an efficient way to enhance the photocatalytic efficiency of Bi_2SiO_5 as GO and AgBr have been proven to be an electron mediator in the formation of heterojunction photocatalysts. The structure, morphology, photoelectric effect, and optical properties were evaluated using spectroscopy techniques such as XRD, FTIR, SEM-EDX, XPS, BET, diffuse reflectance spectra (DRS), photoluminescence (PL), electrochemical impedance spectroscopy (EIS), Mott–Schottky, and photocurrent tests. At the same time, the photocatalytic activities of the heterojunction photocatalyst for the degradation of tetracycline and rhodamine B were investigated and discussed. Moreover, the results were used to deduce the heterojunction GO/BSO/AgBr formation mechanism. This study contributes to the understanding and investigating photocatalysts that can provide sustainable solutions for environmental remediation.

2. Experimental section

2.1. Materials

All chemicals and reagents used were of analytical grade. Bismuth (III) nitrate pentahydrate ($Bi(NO_3)_3.5H_2O$, AR), Silver nitrate ($AgNO_3$, AR), absolute ethanol (C_2H_5OH, AR), sodium bromide (NaBr, AR), sodium silicate nonahydrate (Na_2SiO_3-$9H_2O$, AR), and ethylene glycol ($(CH_2OH)_2$, AR), Isopropyl alcohol (IPA), benzoquinone (BQ), ethylenediaminetetraacetate salt (EDTA-2Na), NaOH, rhodamine B and tetracycline ciprofloxacin were supplied by Sigma-Aldrich, South Africa.

2.2. Photocatalyst preparation

2.2.1. Synthesis of Bi_2SiO_5 nanoparticles

Bi_2SiO_5 nanoparticles were prepared using the hydrothermal method. 2.5 mmol of $Bi(NO_3)_3.5H_2O$ was ultrasonically dissolved in 50 mL ethylene glycol to get a uniform solution A, while 2 mmol of $Na_2SiO_3.9H_2O$ dissolved in 20 mL of distilled water was added dropwise to solution A under vigorous stirring with the resulting mixture stirred for 30 min at room temperature. The mixture was then transferred into a 100 mL Teflon-lined stainless-steel autoclave and heated at 180 °C for 16 hr. The precipitates formed after cooling to room temperature were collected through centrifugation, washed several times with distilled water-ethanol, and dried in an oven at 70 °C overnight to remove any impurities.

2.3. Synthesis of silver bromide (AgBr) nanoparticles

One gram (1 g) of $AgNO_3$ was dispersed in 100 mL of distilled water and stirred in the dark for 30 min. A solution of 0.5 g NaBr dissolved in distilled water was added dropwise, stirring the mixture for an additional 1 hr. The obtained precipitate of AgBr was washed several times with distilled ethanol to remove unreacted chemicals before drying it in the oven overnight.

2.4. Synthesis of GO/Bi_2SiO_5/AgBr nanocomposites

GO/Bi_2SiO_5/AgBr nanocomposites were prepared via an in-situ precipitation process where 0.5 g of the synthesized Bi_2SiO_5 was dissolved in 100 mL absolute ethanol using the ultrasonication method for 30 min. 0.22 g of NaBr and 0.38 g $AgNO_3$ solutions dispersed in 20 mL deionized water, respectively, were added to the Bi_2SiO_5 solution, while 0.05 g solution of graphene oxide GO prepared from the modified Hummers method was added dropwise to the above-dispersed solution while stirring and stirred for additional 2 hr in the dark. Lastly, the obtained product was washed with ethanol and water several times through centrifugation and dried at 60 °C overnight to get the nanocomposites denoted as GO/BSO/AgBr. The Bi_2SiO_5/AgBr composite was also obtained through the same method without adding GO.

2.5. Characterization

Using a PANalytical X′Pert Pro powder X-ray diffractometer in θ–θ configuration and Cu-Kα radiation (ʎ=1.789 Å), the crystalline phase composition of the synthesized nanocomposites was determined. Using the KBr pellet technique, the FTIR spectra of the photocatalyst samples were recorded on a PerkinElmer Spectrum One spectrometer. Brunauer–Emmett–Teller (BET) micrometrics Tristar II 3020 Version 3.02 system evaluated the nanocomposites' specific surface area and pore distribution. The JEOL Scanning Microscope JSM-6400, which is equipped with EDS methods, was utilized for imaging and elemental composition analysis while Kratos Axis supra+ coupled with a monochromatic Al Ka (hv = 1486.6 eV) and running at 150 W were used to obtain the X-ray photoelectron spectroscopy (XPS) of the nanocomposites. A UV–vis spectrophotometer (Agilent Technologies Cary 60 UV–vis, Malaysia) was used to assess the nanocomposites' light absorption performance, and an Autolab Potentiostat (PGSTAT204, Netherlands) workstation was used to measure the synthesized heterostructure composites' electrochemical impedance spectroscopy (EIS), Mott Schottky response, and photocurrent response.

2.6. Electrochemical characterization

The photoelectrochemical properties of the synthesized

photocatalysts ' were assessed using a conventional three-electrode cell with the anode containing the semiconductor, platinum wire, and Ag/AgCl (3.0 M KCl) serving as the working, counter, and reference electrodes, respectively. The working electrode was fabricated by coating a 1.5 cm by 1.5 cm geometric area of fluorine-doped tin oxide (FTO) substrate with 30 mg of the synthesized materials, 5 mg PVDF, and 100 µL NMP as a binder. For the study of the electrochemical impedance spectroscopic analysis, 5 mM $[Fe(CN)_6]^{3-}/[Fe(CN)_6]^{4-}$ in 0.1 M KCl was used. The acquired data was analyzed using the Randle circuit model. In 0.1 M Na_2SO_4, the photocurrent density was measured, and 5 mM $[Fe(CN)_6]^{3-}/[Fe(CN)_6]^{4-}$ solution in a 0.1 M KCl electrolyte was used for the Mott-Schottky experiments, which were carried out in the dark with an applied bias potential of 1.5 V relative to the Ag/AgCl reference electrode.

2.7. Reactor set-up for photocatalytic experiment

The reactor setup was previously described by Ichipi, Tichapondwa [33]. The experimental set-up consists of a wooden box with four Philips 18 W fluorescent daylight lamps to emit visible light irradiation, each emitting a luminous flux of 1200 lm. The inner side of the wooden box was lined with aluminum foil paper to allow for even distribution and reflection of light. Three magnetic stirrers were placed inside the box to about 10 cm from the lamps to continuously stir three batches of the slurry solution. The wattage of the fluorescent lamps and the distance between the reactor and the lamp were used to calculate the light intensity in the photocatalytic reaction to give 142.86 W/m^2. In contrast, the temperature of the reaction set-up was monitored using a thermometer placed inside the wooden box to read a temperature of 30 ∘C (± 5).

For the degradation of the organic pollutants, 50 mg of the synthesized photocatalyst of BSO, AgBr, and GO/BSO/AgBr was dispersed in a solution of tetracycline (100 mL, 30 mg/L, pH 5.5), and Rhodamine B (100 mL, 5 mg/L, pH 5.7) and illuminated using a commercial fluorescent lamp at room temperature, about 5 mL aliquots of the illuminated photocatalyst–pollutant suspension. Mixtures were withdrawn at 10 min, 5 min intervals for 60 min, and 30 min reaction times to evaluate tetracycline and Rhodamine degradation, respectively. The withdrawn aliquots were centrifuged to remove the composite photocatalysts from the treated solutions, filtered through a 0.45 µm membrane filter to remove residual catalyst particulates, and analyzed on UV–vis spectrophotometer (Biochrom, Cambridge, UK) to determine the degradation concentration of the pollutants. A Shimadzu TOC-V analyzer was used to quantitatively assess the extent of TCN and RhB mineralization before and after the photocatalytic reaction.

The photocatalyst's photocatalytic efficiency for the degradation of pollutants was calculated using the following equation:

$$\text{Removal efficiency} = \frac{C_0 - C}{C_0} \times 100\% \quad (1)$$

C0 stands for the concentration of the pollutants at the time (t_0) (initial time) before treatment, while C is the concentration value at the final time after treatment.

3. Results and discussion

As shown in Fig. 1**(a)**, the X-ray diffraction (XRD) patterns of BSO, AgBr, BSO/AgBr, GO, and GO/BSO/AgBr heterostructure photocatalysts are provided to reveal the crystallinity and phase structures of the synthesized materials. It can be seen that the prominent diffraction peaks at 2θ values of 13.53 °, 27.85 °, 33.85 °, 38.61 °, 41.40 °, 44.19 °, 48.44 °, 56.14 °, 57.97 °, 63.45 °, 67.28 °, 71.07 °, 72.04 °, 76.71 °, 93.22 ° and 97.31° were in good accordance with miller indices (hkl) (200), (310), (311), (020), (002), (600), (511), (420), (402), (022),

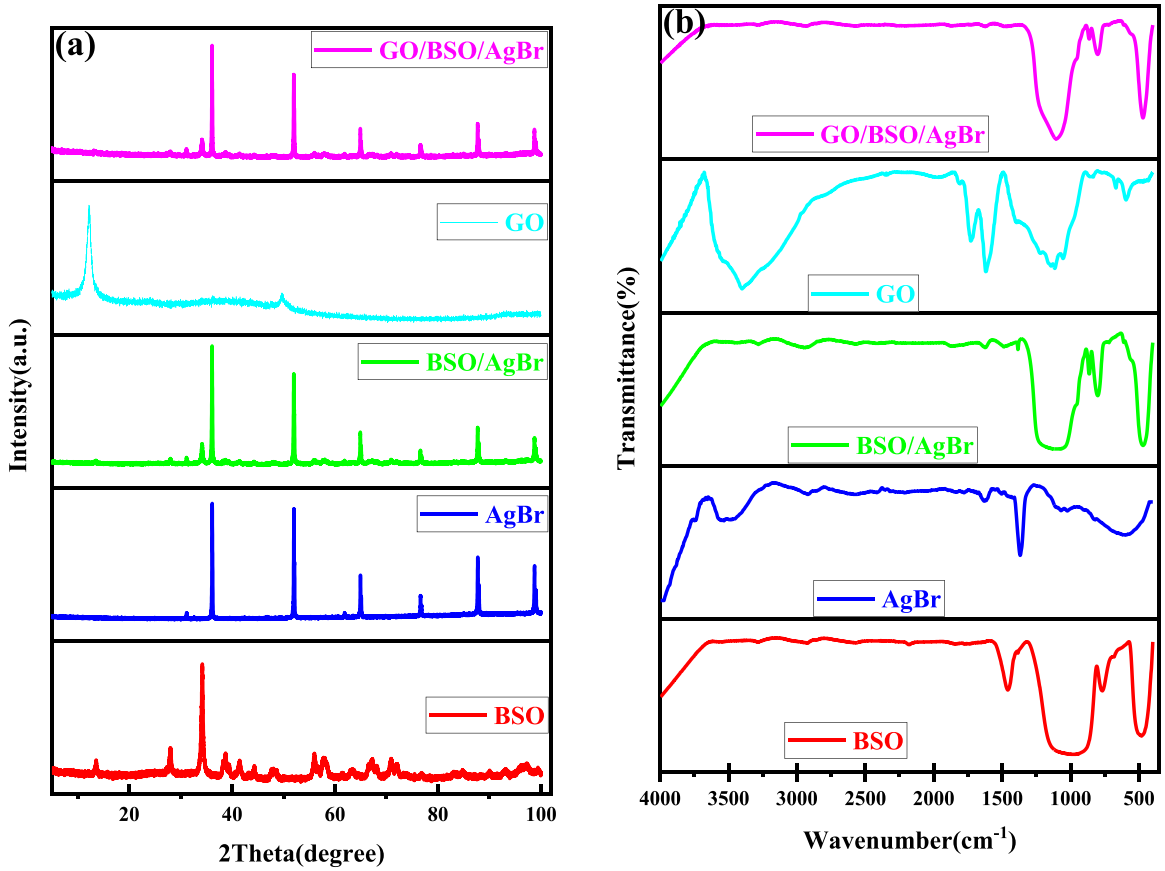

Fig. 1. (a) XRD patterns and (b) FTIR spectral of pristine BSO, AgBr, BSO/AgBr, GO and GO/BSO/AgBr heterojunctions.

(620), (621), (330), (331), (313), and (911) crystal planes of orthorhombic Bi_2SiO_5 (JCPDS No. 36–0287) [25]. The diffraction peaks at 2θ values of 31.16 °, 35.92 °, 52.19 °, 64.87 °, 76.56 °, 87.90 ° and 98.68 ° were indexed to the hkl plane (111), (200), (220), (311), (222), (400), and (422) which are in are in good concurrence with standard data of cubic phase AgBr (JCPDS No. 08–0473) [34]. The existence of the diffraction patterns of Bi_2SiO_5 and AgBr were found in the XRD pattern of BSO/AgBr and GO/BSO/AgBr heterojunction photocatalysts, and this indicates that the BSO/AgBr and GO/BSO/AgBr heterojunction photocatalysts are obtained through the in-situ transformation of GO and Bi_2SiO_5 into AgBr due to the oriented diffusion of Br^- and the subsequent reaction with Ag^+ on the surface of Bi_2SiO_5 [35]. Moreover, it can be seen that no diffraction peaks of GO are observed in the patterns of GO/BSO/AgBr, which could be due to the intense peaks of BSO, AgBr and a low amount of GO concentration in the GO/BSO/AgBr composites.

FTIR spectroscopy was used to evaluate the molecular structures of

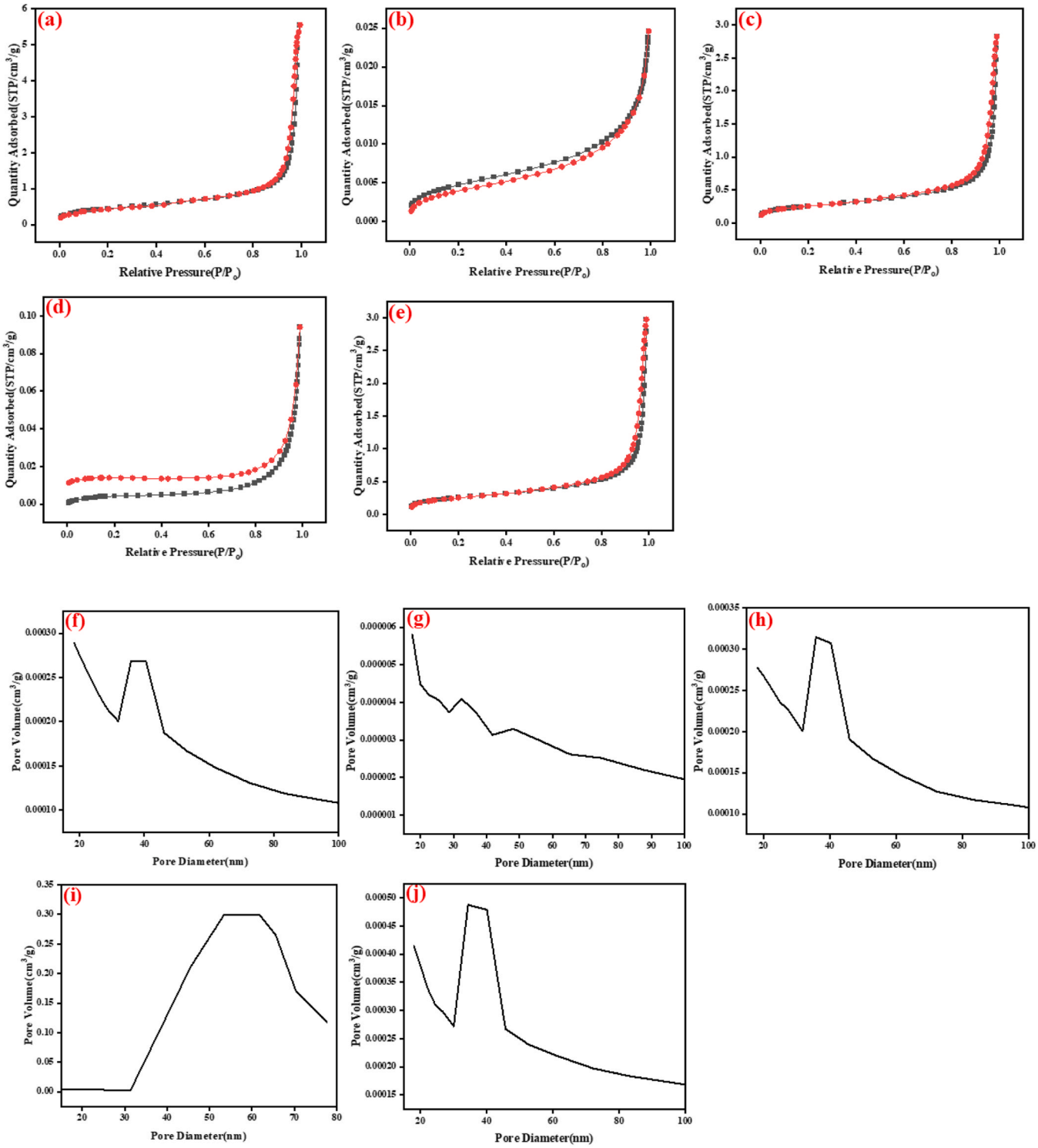

Fig. 2. N_2 adsorption/desorption isotherms of (a)BSO, (b)AgBr, (c)BSO/AgBr, (d)GO, (e)GO/BSO/AgBr and pore size distribution plot of (f)BSO, (g)AgBr, (h)BSO/AgBr, (i)GO, (j)GO/BSO/AgBr.

photocatalysts. For pristine Bi_2SiO_5, the peaks located at around 485, 856, 945, and 1235 cm^{-1} are assigned to the stretching vibration mode of Bi−O bonds, Bi−O−Si bonds, the isolated $(SiO_5)^{6-}$ groups, and the Si−O bonds, respectively [36]. For the AgBr composites, prominent peaks at 3450, 1630, and 1382 cm^{-1} are related to the O–H stretching, H–O–H bending, and OH deformation modes due to the adsorbed water molecules on the surface of the samples, while the infrared spectrum at around 578 cm^{-1} is ascribed to Ag-Br vibration [37]. The BSO/AgBr and GO/BSO/AgBr composite sample shows the characteristic absorption peaks of both Bi_2SiO_5, AgBr, and GO, thereby confirming the existence of Bi_2SiO_5, AgBr, and GO in the synthesized heterostructure photocatalyst.

Fig. 2 shows N2 adsorption/desorption isotherms, BJH pore volume, and size distribution of BSO, AgBr, BSOAgBr, GO, and GO/BSO/AgBr photocatalyst composites. It can be seen from Fig. 2 that all isotherms exhibit type IV physical adsorption isotherms with H3 hysteresis rings, which can be attributed to mesoporous materials [38].

Table 1 shows the synthesized photocatalyst materials' specific surface areas, pore volume, and diameter.

The BET analysis unveiled that the specific surface area, volume, and pore diameter of BSO measured at was 20.50 m^2/g,0.00027 cm^3/g, and 38.34 nm while that of AgBr is measured at 0.40 m^2/g, 0.0000037 cm^3/g, and 40.23 nm with a slight improvement in the surface area of BSO when doped with AgBr (21.46 m^2/g). However, the heterostructure composites of GO/BSO/AgBr possess a superior surface area, volume, and pore diameter of 47.44 m^2/g, 0.00050 cm^3/g, and 45.04 nm, respectively. This shows that the heterostructure composites of GO/BSO/AgBr will generate more surface-active sites during the photocatalytic process for the degradation of organic pollutants.

The surface morphologies of BSO, AgBr, BSO/AgBr, GO, and GO/BSO/AgBr heterostructure composites were analyzed by scanning electron microscopy (SEM); the results are shown in Fig. 3. As shown in Fig. 3**a**, BSO displayed a sheet-like morphology with disordered irregular particles while the AgBr nanoparticle shown in Fig. 3**b** exhibited an irregular spherical structure associated with aggregated particles. It can be seen that the particles of BSO appeared to agglomerate on the surface of the AgBr to form nanosheets. The layer stack of graphene oxide sheets is seen to be indexed within the BSO/AgBr composites, which serves as a matrix for the effective adsorption of the semiconductor composites. EDS analysis (Fig. 3**f**) shows the distribution of elements attributable to Bi, Si, Br, Ag, C, and O, indicating that the synthesized are made up of BSO, AgBr, and GO components.

The distribution of the elements of the synthesized materials was carried out using energy-dispersive spectrometer (EDS) mapping. The results showed that there was the presence of six elements, Bi, Si, Br, Ag, C, and O, which were evenly distributed in GO/BSO/AgBr heterostructure photocatalysts (Fig. 4), which further illustrated the uniformity of the materials.

XPS evaluation of the synthesized composites of GO/BSO/AgBr were conducted to examine its surface chemical compositions and chemical states were provided and demonstrated in Fig. 5. The full survey spectrum of the composites (Fig. 5**a**) depicts the presence of the following elements Bi, Si, Br, Ag, C and O with binding energies around 166 eV, 104 eV, 183 eV, 369 eV, 286 eV and 534 eV which matches with the EDS analysis confirms the formation of heterojunction within the composites. The Bi 4 f spectrum (Fig. 5**b**) is made up of three peaks centered at 159.3 eV (Bi 4 $f_{7/2}$) and 164.6 eV (Bi 4 $f_{5/2}$), which is indicative of the presence of Bi^{3+} in the synthesized composites while the peak at 154.3 eV (Bi 4 $f_{7/2}$) can be linked to reduced bismuth ions [21,39]. The Si 2p spectrum in Fig showed a strong peak at 103.3 eV, characteristic of Si^{4+}. As shown in Fig. 5**c**, the peak at the binding energy of 68.5 eV is generated by Br 3d, which indicates the presence of Br in the composites. The two distinct peaks at the binding energy of 367.9 eV and 373.9 eV are associated with Ag^+ $3d_{5/2}$ and Ag+ $3d_{3/2}$ [40,41] respectively, which proves the existence of Ag in the form of Ag^+ in the synthesized composites of GO/BSO/AgBr. The spectrum of C 1 s shows peaks at the binding energy of 284.8, 286.4, and 289.3 eV, which are attributed to the C–C, C–O, and C═O bonds, while O 1 s spectrum in Fig. 5**g** with peaks located at a binding energy of around 530.1 and 532.8 eV attributed to the lattice oxygen and adsorbed surface oxygen [27,42,43].

The optical properties of the synthesized composites were evaluated using UV–Vis DRS spectroscopy, while the band gap energy was calculated using the Kubelka-Munk formula. BSO exhibited suitable adsorption properties at the ultraviolet spectrum of the spectroscopy, while AgBr showed good adsorption at the visible light spectrum. The absorption edges are 377 nm, 424 nm, 463 nm, and 534 nm for BSO, AgBr, BSO/AgBr, and GO/BSO/AgBr, respectively. The absorption edge of the heterostructure GO/BSO/AgBr is observed to be a redshift to 534 nm. This can be associated with the addition of owing to its strong visible-light absorption [44].

The band gap of photocatalysts was then calculated according to the formula given below [45]:

$$\alpha hv = A(\nu h - Eg)^{n/2} \quad (2)$$

Therefore, it can be seen from Fig. 6**b** that the bandgap energies of BSO, AgBr, BSO/AgBr, and GO/BSO/AgBr are estimated to be 3.54 eV, 2.84 eV, 2.38 eV, and 2.11 eV, respectively. However, the energy band gap of GO/BSO/AgBr (2.11 eV) is slightly smaller than that of BSO/AgBr (2.38 eV) when GO is introduced in the heterostructure, which is consistent with the trend of light absorption capacity.

The PL spectra of BSO, AgBr, BSO/AgBr, and GO/BSO/AgBr were also evaluated to reveal the recombination rate of the photogenerated carriers of prepared photocatalysts. As shown in Fig. 7**a**, the BSO has a strong and wide PL emission peak centered at 467 nm, which indicates the highest recombination of the photogenerated charge carriers on the pristine BSO, which will definitely result in poor photocatalytic performance[46]. With the introduction of AgBr into BSO, the PL emission intensity of the composites becomes much lower than that of BSO and AgBr, which is indicative that the introduction of AgBr into BSO inhibits the recombination of photogenerated charge carriers. The GO/BSO/AgBr heterostructure shows the least peak intensity, indicating the highest separation efficiency of electron-hole pairs, revealing that the introduction of GO into the heterostructure composite results in more effective charge separation of the photocatalysts with enhanced photocatalytic performance [47].

The photogenerated carrier transfer efficiency and impedance of the synthesized photocatalysts were evaluated using electrochemical impedance spectroscopy (EIS), where the arc radius is proportional to the charge transfer resistance[48,49]. As seen in Fig. 7**b**, the heterostructure composite of GO/BSO/AgBr shows the smallest arc radius, proving that the introduction of GO and AgBr into BSO enhances its photogenerated carrier separation efficiency of composite materials.

In addition, Mott-Schottky (MS) plots were used to assess the flat band potentials (E_{fb}) of BSO and AgBr (E_{fb}). As seen in Fig. 8, the positive slopes of the BSO and AgBr MS curves are explained by the property of n-type semiconductors [50]. The E_{fb} of BSO and AgBr were estimated to be −0.29 V and −0.68 V (vs. Ag/AgCl), respectively, while applying the Nernst equation given as $E_{NHE} = E_{Ag/AgCl} + 0.197$ (pH) [51], the electrode potential of the exact flat band potentials of BSO and AgBr were

Table 1
BET surface areas, pore volumes, and pore size diameter of the materials.

Material	Surface area (m^2 g^{-1})	Pore Volume (cm^3 g^{-1})	Pore Diameter (nm)
BSO	20.50	0.00027	38.34
AgBr	0.40	0.0000037	40.23
GO	298.30	0.30	57.62
BSO/AgBr	21.46	0.00032	41.38
GO/BSO/AgBr	47.44	0.00050	45.04

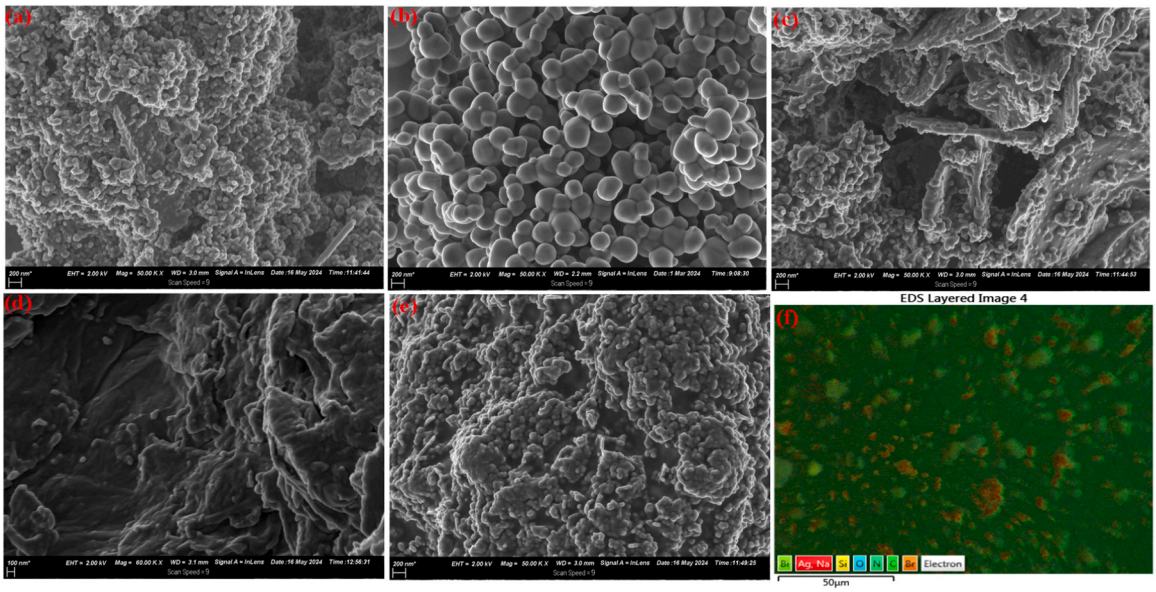

Fig. 3. SEM micrographs of (a) BSO, (b) AgBr, (c) BSO/AgBr, (d) GO, (e) GO/BSO/AgBr and EDS micrograph of GO/BSO/AgBr.

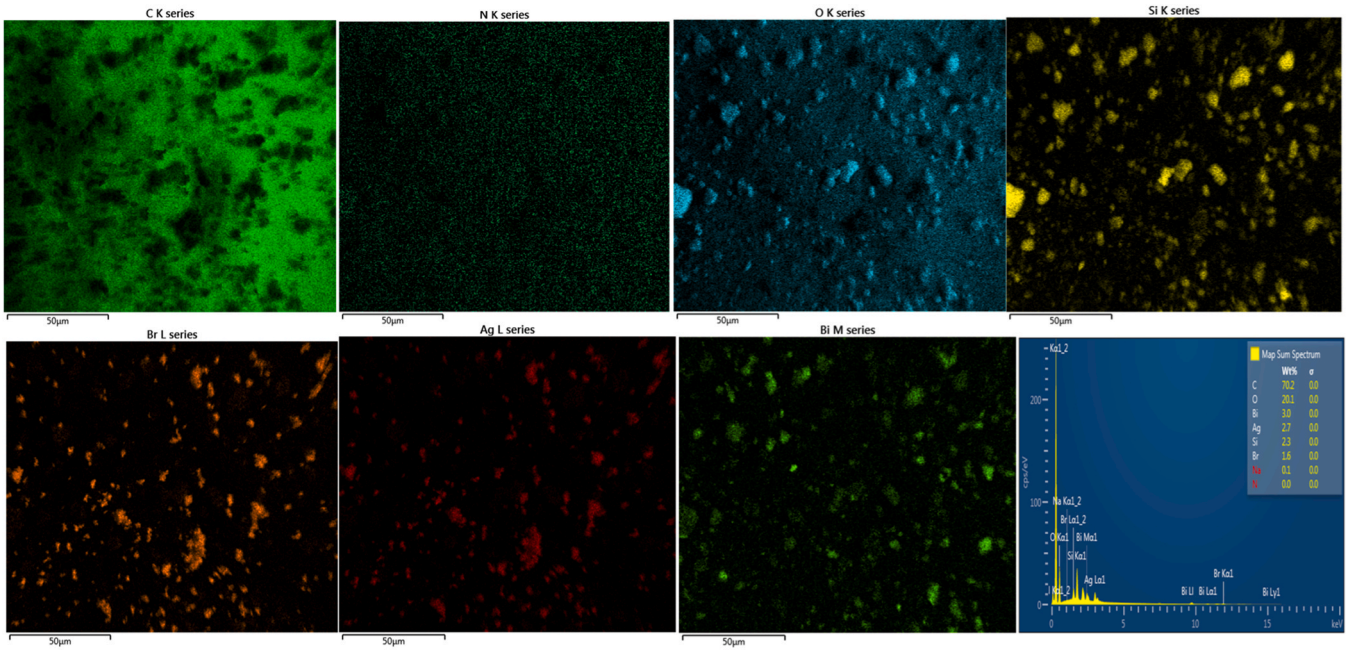

Fig. 4. EDS mapping of the heterojunction GO/BSO/AgBr photocatalyst.

calculated to be −0.09 eV, and −0.48 eV (versus Normal Hydrogen Electrode). Therefore, the conduction band potential (E_{CB}) values of BSO and AgBr are calculated to be −0.11 and −0.28 eV, respectively, since the conduction band potentials (E_{CB}) of n-type semiconductors are approximately 0.2 V more negative than the E_{fb} [52,53]. Finally, when combined with the value from the ultraviolet-visible diffuse reflectance spectroscopy analysis with the band formula given as $E_{VB} = E_g + E_{CB}$ [54], the valence band (VB) positions of BSO and AgBr were calculated to be near 3.31 eV and 2.56 eV (vs. NHE), respectively.

Fig. 9 shows the transient photocurrent response that was carried out to evaluate the effectiveness of photoelectron migration and separation under on-off light irradiation, as the efficiency of electron and hole separation is used to determine the photocurrent's intensity [55,56]. The results clearly indicate that GO/BSO/AgBr exhibits a higher photocurrent intensity than BSO, AgBr, and BSO/AgBr. Additionally, the heterojunction photocatalyst demonstrates an enhanced photocurrent signal that has not decayed when compared to other materials, indicating lower electron-hole recombination.

3.1. Degradation of organic pollutants

Tetracycline (TCN) and Rhodamine B (RhB) were selected as the target pollutants to evaluate the adsorptive and photocatalytic activity of the as-synthesized photocatalyst under visible irradiation. First, the adsorptive performance of the synthesized photocatalysts was assessed through TCN and RhB removal experiments in the dark for 30 and 60 min, respectively. The TCN removal efficiency of GO, BSO AgBr, BSO/AgBr, and GO/BSO/AgBr were approximately 25.13 %, 7.65 %, 2.91 %, 10.25 % and 19.03 % in 60 min, while RhB removal efficiency of GO, BSO AgBr, BSO/AgBr and GO/BSO/AgBr achieved 29.03 %,

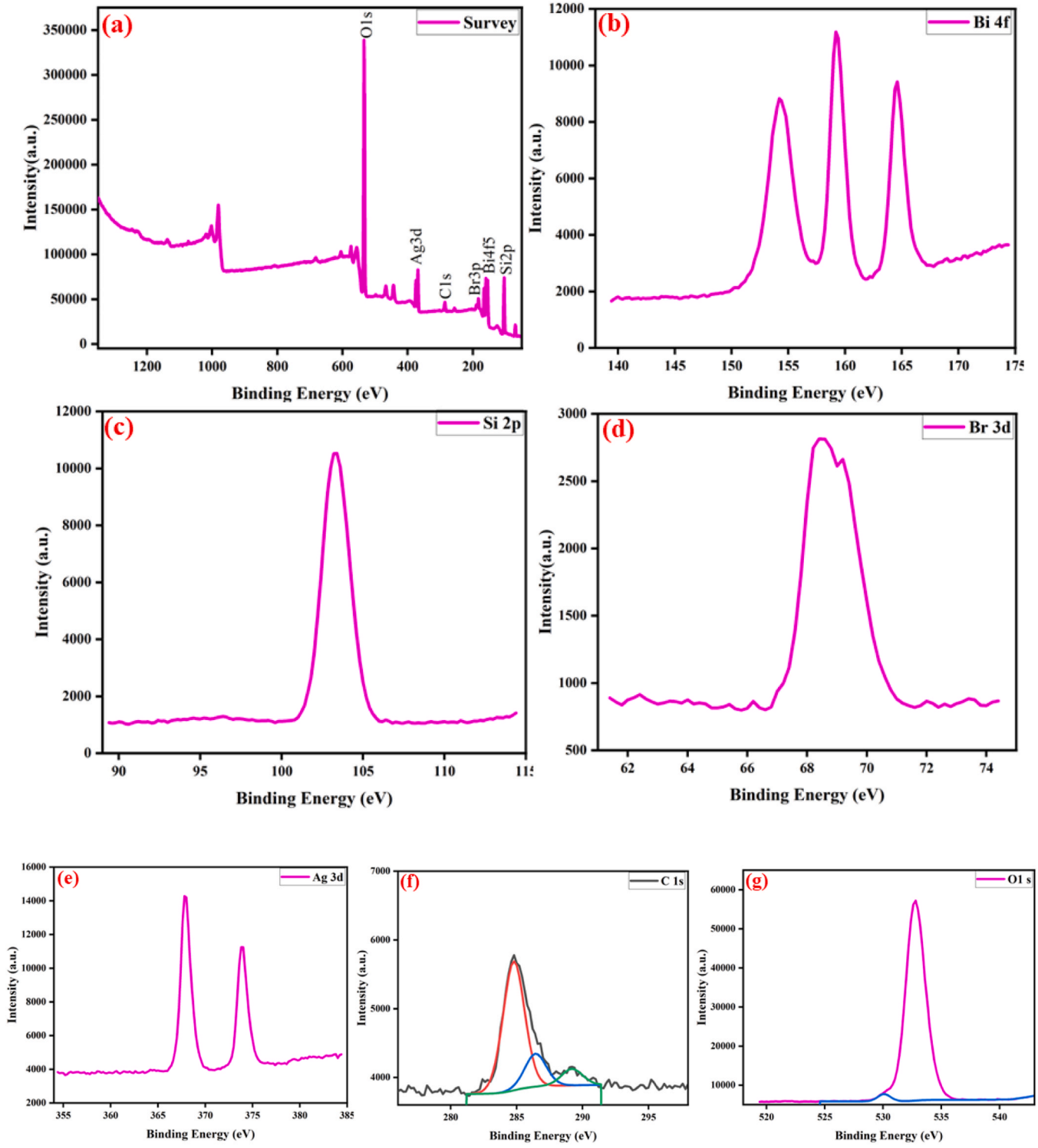

Fig. 5. (a) XPS survey of the GO/BSO/AgBr composite, (b) Bi 4 f, (c) Si 4 f, (d) Br 3d (e) Ag 3d, (f) C 1 s and (g) O 1 s, for the synthesized composites of GO/BSO/AgBr.

11.96 %, 4.07 %, 13.32 % and 21.24 % in 30 min. The obtained results demonstrated that GO has the highest adsorption potential when compared with the other prepared photocatalysts, which can be attributed to the GO's high specific surface area with improved active sites (Table 1).

For the photocatalytic efficiency of the synthesized composites, a dark reaction was carried out for the pollutants. The results show little or no degradation by the photocatalyst in the solution, indicating the establishment of an equilibrium between the contaminants and the photocatalysts. Meanwhile, during the visible light irradiation, the BSO and AgBr photocatalyst composites exhibited a relatively low degradation efficiency of 39.95 % and 58.03 %, 29.23 % and 43.40 % for the removal of TCN and RhB from simulated water, respectively. The low removal efficiency of BSO and AgBr could be due to their low visible light utilization and quantum efficiency, while the composites of BSO/AgBr achieved an improved degradation efficiency of 81.16 % and

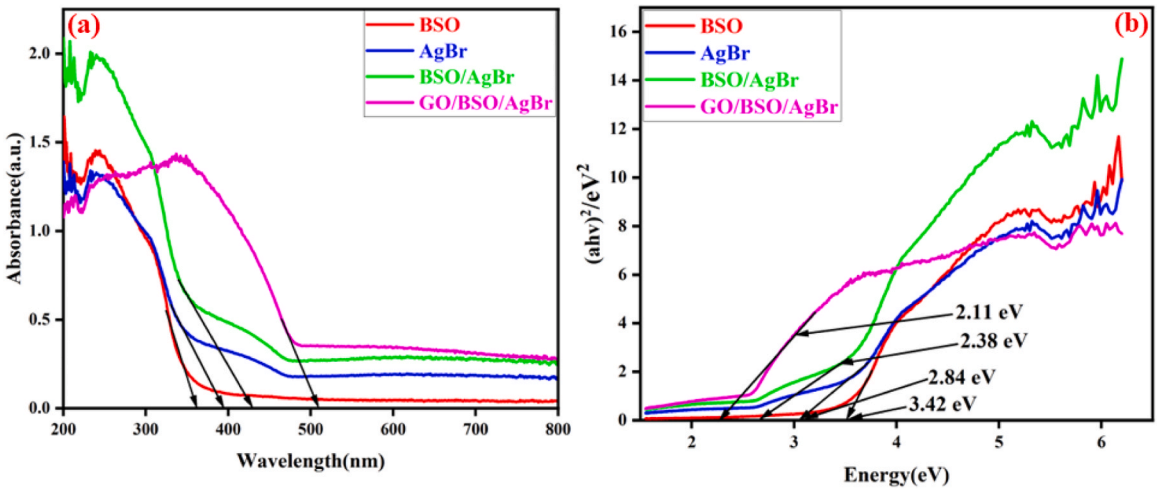

Fig. 6. (a) UV-DRS spectra and Tauc plot for BSO, AgBr, BSO/AgBr, and GO/BSO/AgBr, respectively.

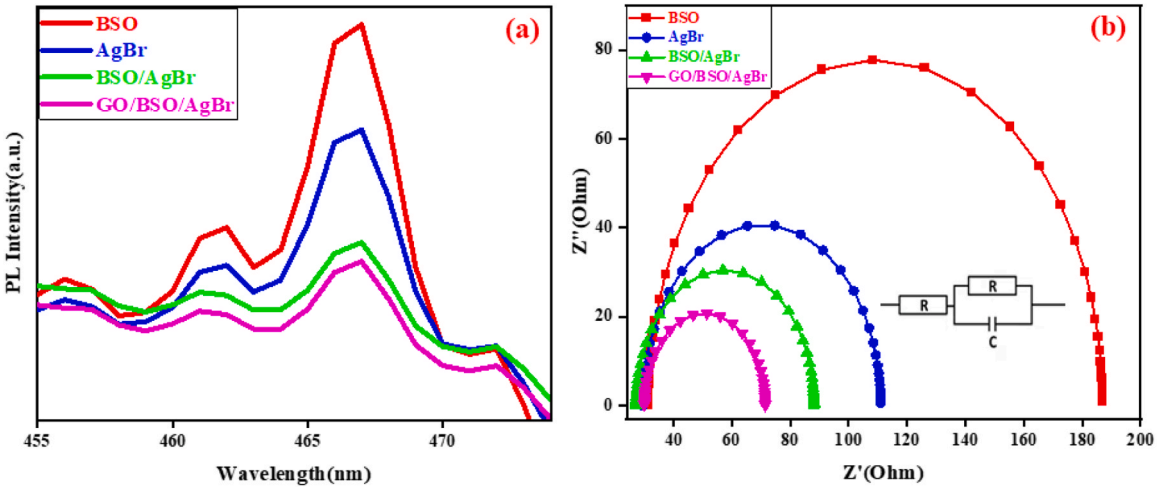

Fig. 7. (a) PL spectra and (b) EIS spectra (fitted Randle circuit) for BSO, AgBr, BSO/AgBr, and GO/BSO/AgBr.

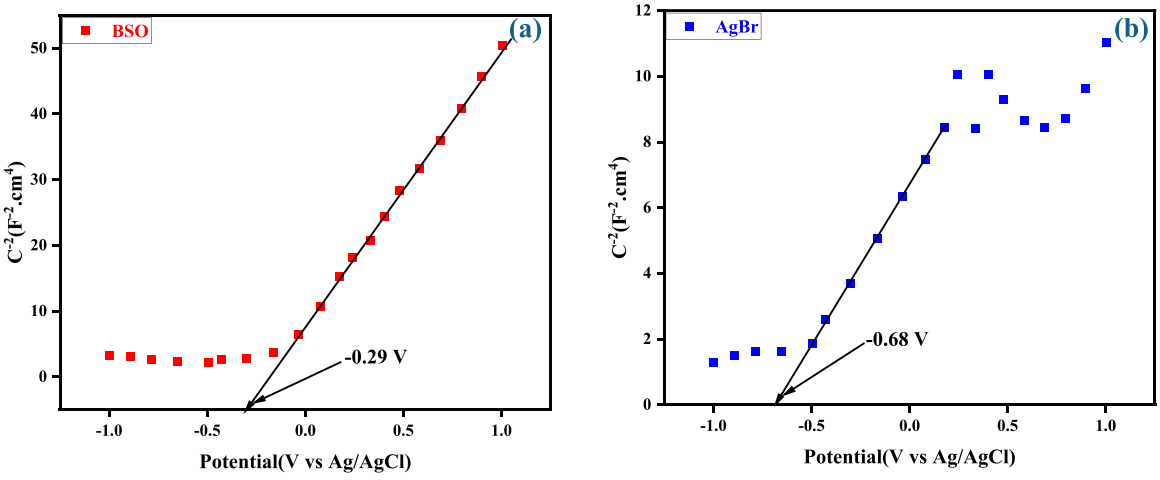

Fig. 8. Mott—Schottky curves of BSO and AgBr.

70.19 % for the degradation of TCN and RhB. There was a substantial improvement in the removal of TCN and RhB after the introduction of GO into the surface of the BSO/AgBr composite up to 95.83 % and 97.02 % under identical conditions as shown in Fig. 11. The synergistic effects between the surface of GO and the BSO/AgBr composites via combined adsorption and photocatalysis under visible light irradiation could be the reason for the improvement in their degradation efficiency. This is possible due to the ability of the synthesized composites of BSO/

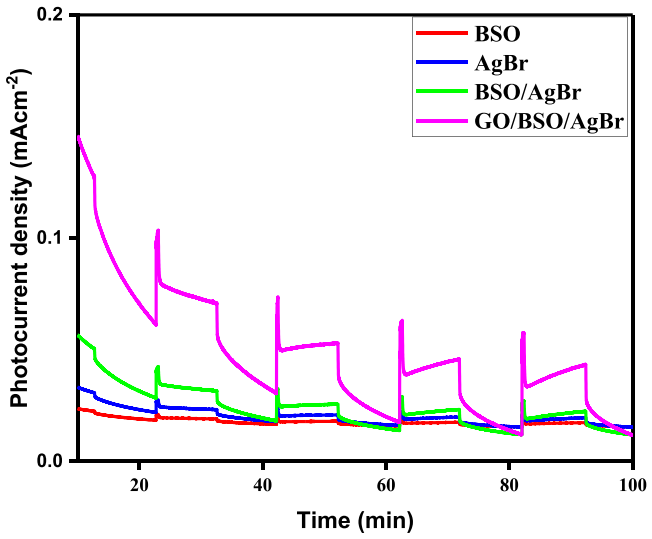

Fig. 9. Photocurrent density of BSO, AgBr, BSO/AgBr, and GO/BSO/AgBr.

AgBr to enhance its quantum efficiency and improve light harvesting efficiency by promoting rapid oxidative reactions of TCN and RhB through the formation of •OH. At the same time, the GO provides specific surface areas that function as active sites for adsorption purposes before irradiation of visible light [57,58].

As shown in Fig. 11**b** and **d,** the degradation kinetics of TCN and RhB aligned with the pseudo-first-order reaction kinetics formula as given below:

$$In(C_o/C) = k_{ap}t$$

Where k_{ap} represents the apparent pseudo-first-order rate constant, *Co* is the initial concentration, and *C* is the pollutant's concentration after light irradiation.

From the calculated results, the reaction rate constant k of the GO/BSO/AgBr shows the fastest reaction time value of 0.03526 min^{-1} and 0.03528 min^{-1} for TCN and RhB, respectively. These results explain that the construction of GO/BSO/AgBr heterojunction photocatalyst with improved morphology could offer convenience in enhancing the photocatalytic efficiency of a single BSO.

Additionally, TOC analysis was used to evaluate the mineralization efficiency of the GO/BSO/AgBr heterojunction photocatalyst for TCN and RhB pollutants (Fig. 12). The results demonstrated the remarkable photocatalytic performance and mineralization potential of the GO/BSO/AgBr heterojunction photocatalyst, showing that 65.95 % and 61.40 % of TOC was removed upon exposure to visible light for TCN and RhB respectively.

In order to evaluate the photocatalytic performance of the synthesized composites of GO/BSO/AgBr heterojunction photocatalyst in this study on TCN and RhB, we collected literature on photocatalytic degradation of TCN and RhB as presented Tables 3 and 4**.** In comparison, the photocatalytic degradation effect of the synthesized photocatalyst composites in this study is better than other photocatalysts for the degradation of TCN and RhB respectively.

3.2. Effect of initial pH on TCN and RhB degradation by GO/BSO/AgBr

The effect of pH is one of the critical factors considered in water treatment applications as it affects the extent of the target pollutant's degradation by the surface of a photocatalyst as their active sites are dependent on the concentration of H^+ or OH^- in aqueous solutions [69]. The optimum pH for TCN and RhB degradation by the GO/BSO/AgBr composites was determined by varying the solution pH from 3 to 11 and 3–11 with hydrochloric acid and sodium hydroxide, respectively.

As shown in Fig. 13**a**, the degradation efficiency of GO/BSO/AgBr at pH =3-11 was 46.76 %, 81.78 %, 96.11 %, 76.18 %, and 57.90 % for the removal of TCN in water. These results can be attributed to the difference between the TCN charges (TCN^{3+}, $TCN^{\pm}$, TCN^-) and the active site of the photocatalyst. The reduction in the degradation efficiency at an acidic medium can be attributed to the positive charge of TCN^{3+} in the solution, which will compete with H^+ in the solution for the active site on the catalyst surface, while the degradation efficiency of TCN was the highest at pH seven which is due to the inhibition of OH and O_2 evolution reaction as a result of the formation of electrostatic force which leads to the acceleration of reaction rate under neutral condition [70,71]. Under alkaline conditions, the degradation efficiency gradually decreases, possibly due to the lack of electrostatic interaction between TCN and the photocatalyst.

As shown in Fig. 13**b**, the degradation rate of RhB was 54.45 %, 69.89 %, 98.71 %, 91.27 %, and 80.97 % at the pH values of 3, 5, 7, 9, and 11 after 30 min. These results show that the carboxyl group of RhB deprotonates and exists in the cation form (RhB^+), repelling the photocatalyst's cationic surface when the pH is in an acidic medium. However, when the pH of the RhB is in the alkaline medium, the surface of the photocatalyst possesses a negative charge, causing repulsion between the anionic form of (RhB^-) and the anionic surface of the photocatalyst with a reduced degradation activity [72,73].

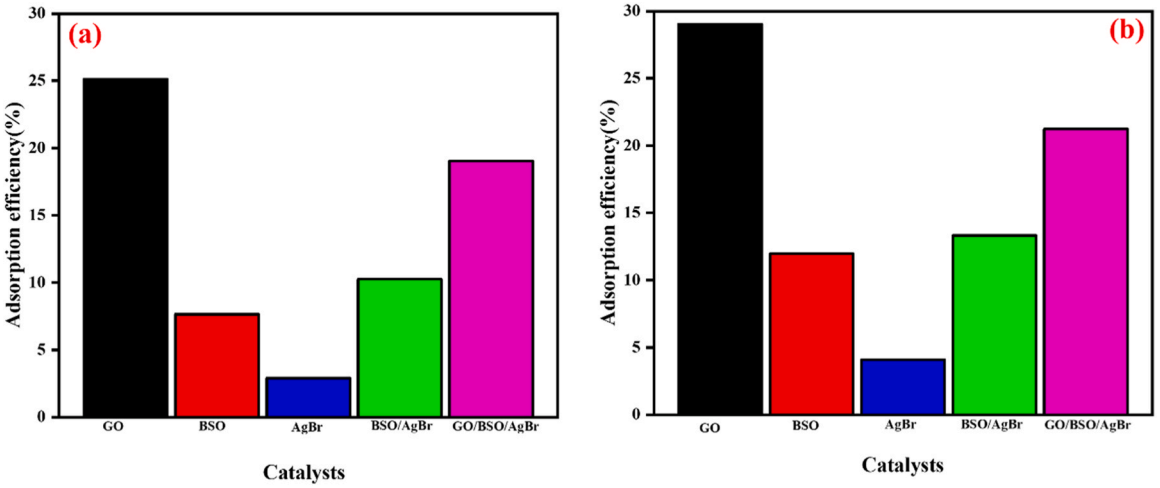

Fig. 10. Adsorption efficiency of TCN(a) and RhB(b) using the synthesized photocatalyst.

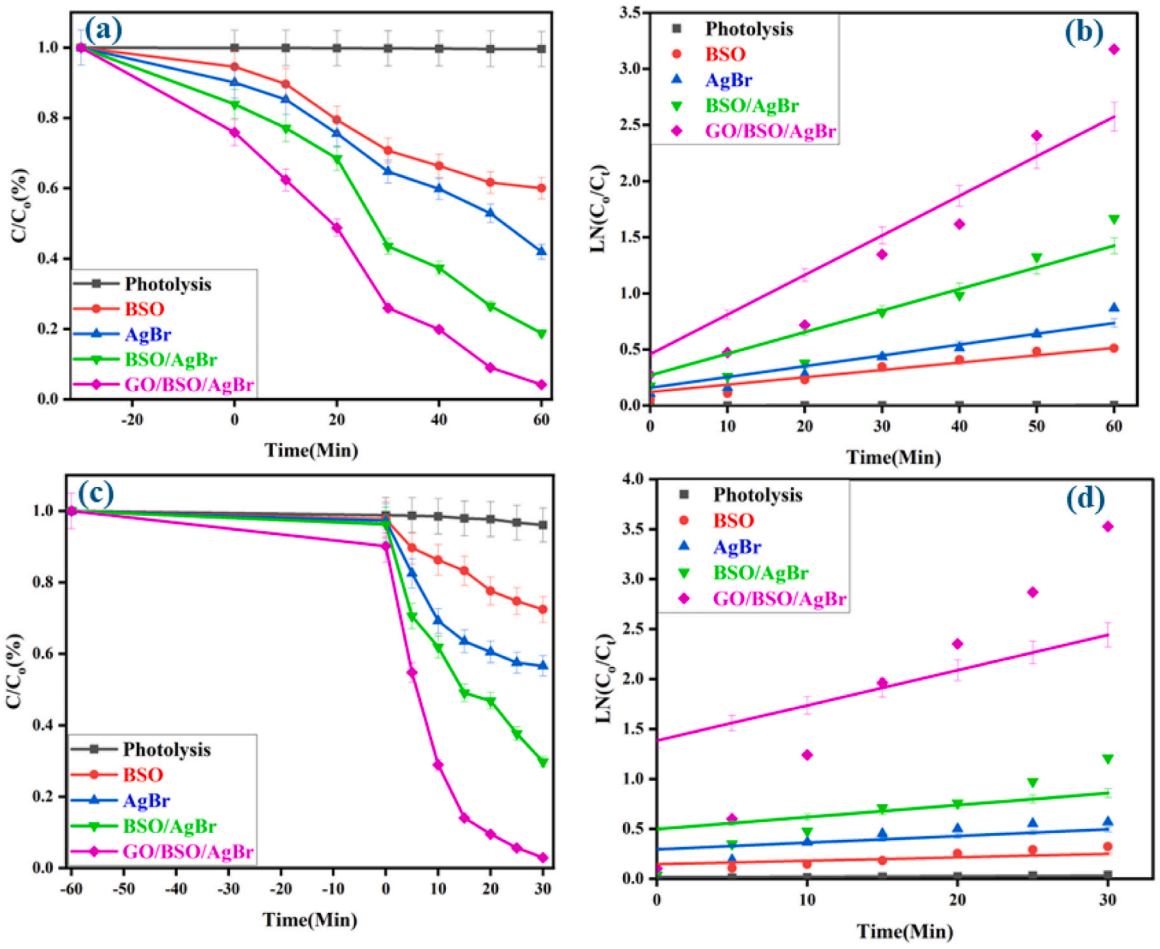

Fig. 11. (a) photocatalytic degradation of TCN, (b) kinetics plot of TCN degradation, (c) photocatalytic degradation of RhB, and (d) kinetics plot of RhB using the synthesized photocatalysts.

Table 2
The photodegradation efficiency and reaction rate constant k for TCN and RhB of all as-prepared photocatalyst.

Photocatalyst	TCN		RhB	
	Degradation rate (%)	k^{-1}	Degradation rate (%)	k^{-1}
BSO	39.95	0.00655	29.23	0.00343
AgBr	58.03	0.00963	43.40	0.00665
BSO/AgBr	81.16	0.01923	70.19	0.01203
GO/BSO/AgBr	97.02	0.03526	95.83	0.03528

3.3. Dosage of the photocatalyst

The GO/BSO/AgBr dosage that affects the degradation of TCN and RhB under visible light was investigated. Five doses of the photocatalyst at 10 mg, 30 mg, 50 mg, 70 mg, and 90 mg were applied to degrade TCN and RhB. As shown in Fig. 14, under the same photocatalytic conditions, the TCN and RhB achieved 74.36 %, 83.10 %, 95.82 %, 90.78 %, 69.97 %, and 83.12 %, 92.12 %, 97.08 %, 90.06 %, 85.88 % degradation efficiencies. The degradation rate increases with an increase in the catalyst dosage, which is attributable to generating more free radicals and active sites on the catalyst surface [73,74]. The decrease in degradation efficiency above dosages of 70 mg and 90 mg can be linked to the aggregation between the photocatalyst and the pollutants, reducing its active surface area.

The stability of the GO/BSO/AgBr composites was conducted to confirm the sustainability of the photocatalytic process for practical applications. From Fig. 15**a**, it can be seen that the GO/BSO/AgBr composite catalyst still possesses a high photocatalytic activity for the degradation of tetracycline after being recycled five times with a degradation efficiency of 86.47 %. The morphology of the GO/BSO/AgBr composite catalyst, after being recycled five times, exhibits negligible deviations from its initial state, while the XRD pattern of the composite catalyst after five repeated uses shows no significant change in the characteristic peak, suggesting the preserved structural phase of the composites when compared to the initial catalyst. The findings show that the composite catalyst exhibits remarkable stability and reusability, offering a practical wastewater treatment approach.

The quenching experiment was carried out to evaluate the main active substances generated during the degradation process. Substances such as isopropanol (IPA), ethylenediaminetetraacetic acid (EDTA), and benzoquinone (BQ) were added into the solution as scavengers for $^{\bullet}OH$, h^{+}, $^{\bullet}O_2^{-}$ respectively [75,76]. The degradation efficiency reached 82.94 % with the addition of IPA, which shows that the photocatalytic activity is not significantly inhibited during the photocatalytic process, indicating that $^{\bullet}OH$ plays a minor role. The addition of EDTA and BQ remarkably inhibited tetracycline degradation to 36.05 % and 27.71 %, with the resulting showing that h+ and $\bullet O_2^{-}$ contributed majorly to the photocatalytic degradation of tetracycline for the GO/BSO/AgBr photocatalyst under visible light irradiation.

3.4. Proposed mechanism

The photosensitization of organic pollutants occurs when synergistic effects are created between a pollutant and photocatalysts under visible

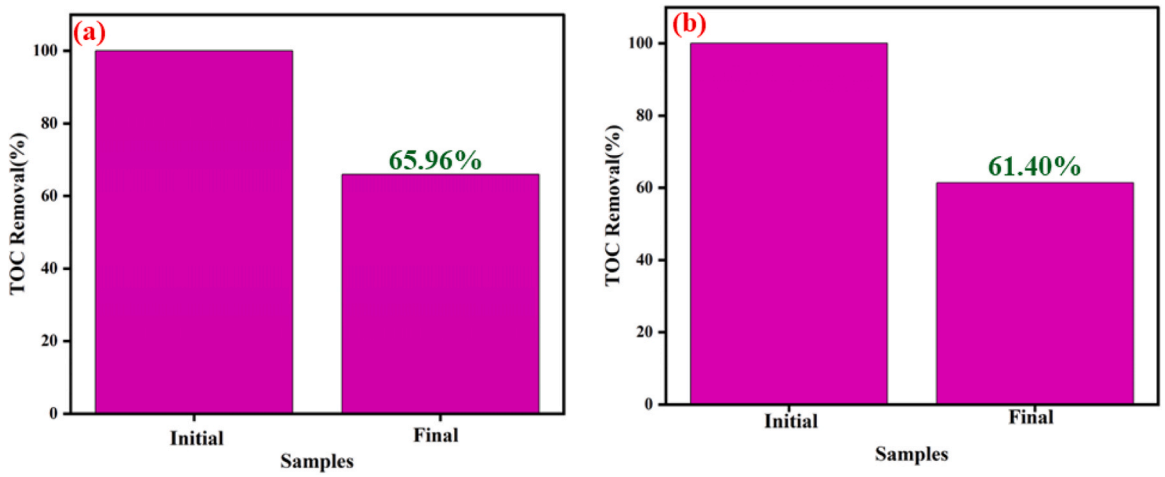

Fig. 12. TOC removal rate for TCN and RhB.

Table 3
Comparison table for degradation of TCN with different synthesized photocatalyst.

Photocatalyst	Light source	Dosage	Amount/mg/L	Photocatalytic efficiency	Reference
g-C_3N_4/STI−6	500 W xenon lamp	2 g/L	30	86.8 % in 4 hr	[59]
Ag/g-C_3N_4@CL	Simulated solar light	1.0 g/L	15	87.2 % in 3 hr	[60]
Ag_2CO_3/TiO_2/ SiC	300 W xenon lamp	0.2 g/L	10	95.9 % in 30 min	[61]
SnO_2/g-C_3N_4	250 W xenon lamp	50 mg/L	30	95.9 % in 2 hr	[48]
Co_3O_4/g-C_3N_4	350 W xenon lamp	20 mg/L	15	85.3 % in 2 hr	[62]
$La_{0.7}Sr_{0.3}MnO_3$/g-C_3N_4	350 W xenon lamp	0.05 g	50	95.0 % in 3.5 hr	
La-FeCo-Doped $SrTiO_3$/TiO_2	Mercury lamp	1.6 mg	20	99.1 % in 2 hr	[63]
GO/BSO/AgBr	72 W fluorescent daylight lamps	50 mg	30	97.02 % in 1 hr	This study

Table 4
Comparison table for degradation of RhB with different synthesized photocatalyst.

Photocatalyst	Light source	Dosage	Amount/mg/L	Photocatalytic efficiency	Reference
Ag/GO/g-C_3N_4	500 W xenon lamp	50 mg/L	10	99.5 % in 2 hr	[64]
g-C_3N_4/ZrO_2	natural sunlight irradiation	50 mg/L	10	94.1 % in 1.5 hr	[65]
TiO_2-GO-AgNs	150 W xenon lamp	50 mg/L	10	93.0 % in 5 hr	[66]
$SnIn_4S_8$/$SmVO_4$	300 W halogen lamp	0.8 g/L	8	97.6 % in 45 min	[67]
Bi_2SiO_5/Ag/AgBr	500 W xenon lamp	20 mg/L	10	96.6 % in 30 min	[30]
$AgVO_3$/BiOI	250 W tungsten halogen lamp	75 mg/L	10	91.0 % in 1.5 hr	[68]
GO/BSO/AgBr	72 W fluorescent daylight lamps	50 mg/L	5	95.83 % in 30 min	This study

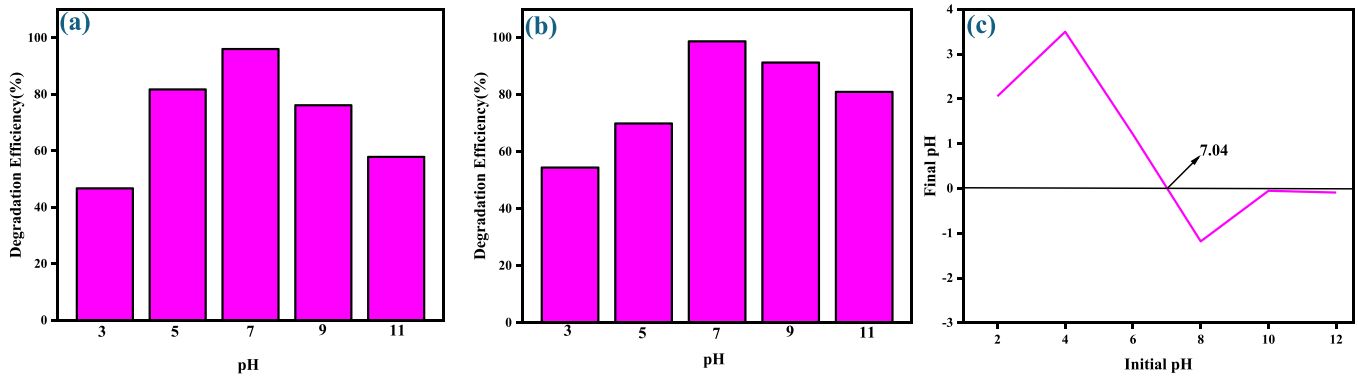

Fig. 13. Degradation curves of TCN and RhB at different pH.

light irradiation to generate electron-hole pairs. The generated electron-hole pairs can react with water molecules to form reactive species like hydroxyl (•OH) and superoxide ($\bullet O_2^-$) radicals that can oxidize pollutants like TCN and RhB, breaking them into harmless products. Therefore, based on the result obtained from UV–Vis spectroscopy and the Mott—Schottky plot method, the calculated band gaps of BSO and AgBr were 3.42 eV and 2.63 eV. From the Mott–Schottky analysis, the energy positions of the conduction band (CB) and valence band (VB) of BSO are calculated to be −0.11 eV and + 3.31 eV, and that for AgBr is calculated to be −0.28 eV and 2.56 eV, respectively. Upon irradiation, electrons

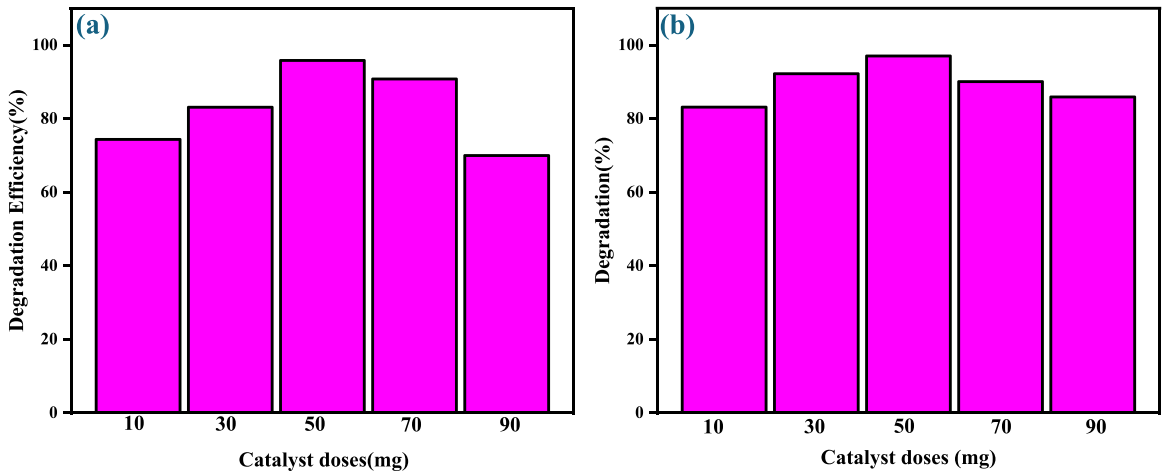

Fig. 14. Degradation curves of TCN and RhB at different catalyst doses.

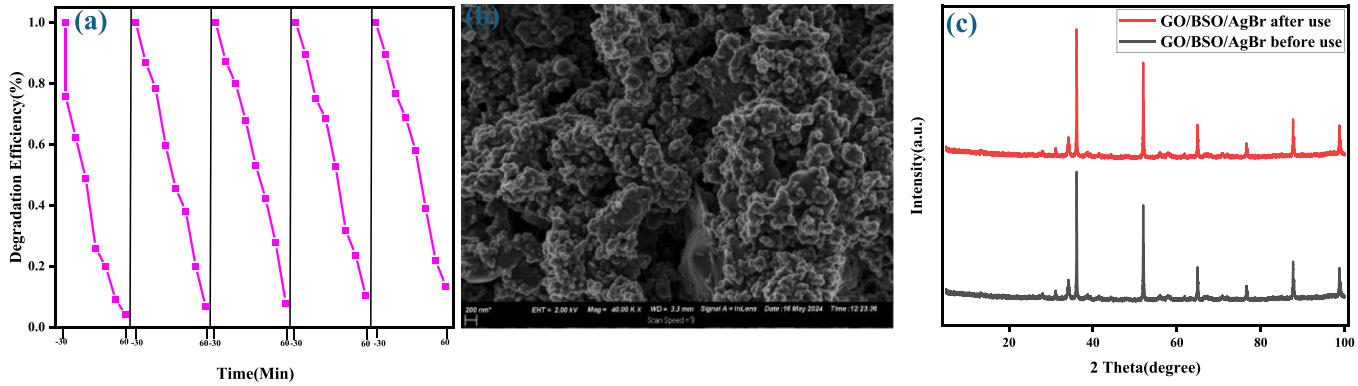

Fig. 15. (a) Recycling performance of GO/BSO/AgBr for the degradation of tetracycline, (b) SEM image, and (c) XRD patterns of fresh and used GO/BSO/AgBr.

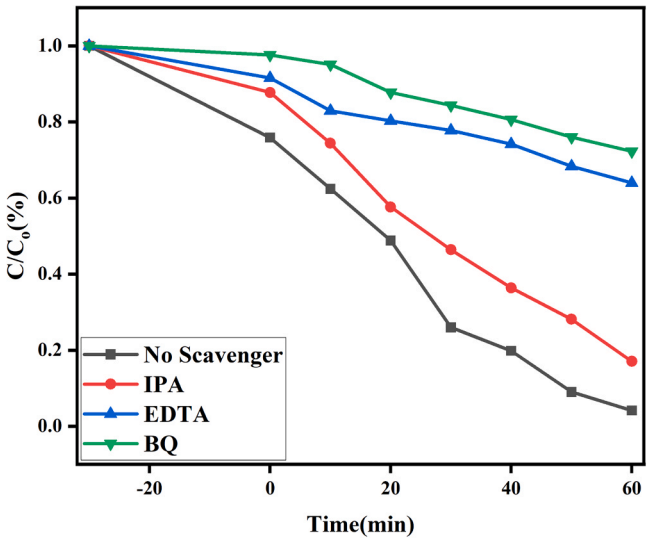

Fig. 16. Free radical capture experiment for the degradation of TCN using GO/BSO/AgBr.

and holes are generated by the transfer of electrons to the GO sheets on the GO/BSO/AgBr heterojunction. This produces a low recombination rate and is thermodynamically favorable, allowing the adsorption of the pollutant molecules (TCN and RhB) on a better platform and separating photo-generated e^-/h^+ pairs [77,78]. The photoexcited electrons in the CB of AgBr will prefer to be transferred to the CB of BSO. In contrast, the photoexcited holes will prefer to be transferred from the VB of BSO to the VB of AgBr due to the potential difference caused by their different energy band levels. As a result, the AgBr SPR feature allows photo-generated electrons to be transferred to the TCN and RhB solution through the GO's surface, effectively separating the photoexcited charge carriers and improving their photocatalytic activity.

Moreover, the CB potential of BSO (-0.11 eV vs. NHE) and CB potential of AgBr (-0.28 eV vs. NHE) is more positive than the standard potential of $O_2/^{\bullet}O_2^-$ (-0.33 eV vs. NHE), which is indicative that O_2 could not be easily reduced to $^{\bullet}O_2^-$ by the photoexcited electrons while the quenching experiment provided that h^+ and $^{\bullet}O_2^-$ are the active species in the photocatalytic system. Therefore, the addition of GO will improve the visible light absorption of the binary composites of BSO/AgBr and create additional active sites that engage with organic pollutants. Furthermore, due to its high conductivity, it will serve as an electron transport channel between BSO and AgBr, resulting in an increased electron transfer rate. This enhancement will extend free electrons' lifespan, which boosts superoxide generation, thereby offering more chances for their participation in degradation processes [79,80]. The photogenerated h+ in the VB of BSO and AgBr could directly degrade TCN and RhB molecules and react with H_2O to produce •OH because the VB edge potential of BSO (+3.31 eV vs NHE) and VB edge potential of AgBr (+2.56 eV vs NHE) is more positive than the potential $H_2O/•OH$ (+1.99 eV vs NHE) [81,82]. This proposed mechanism aligned with the scavenging experiment, which proves that h^+ and $^{\bullet}O_2^-$ are the main active species in the photodegradation of TCN and RhB over the synthesized GO/BSO/AgBr heterojunctions.

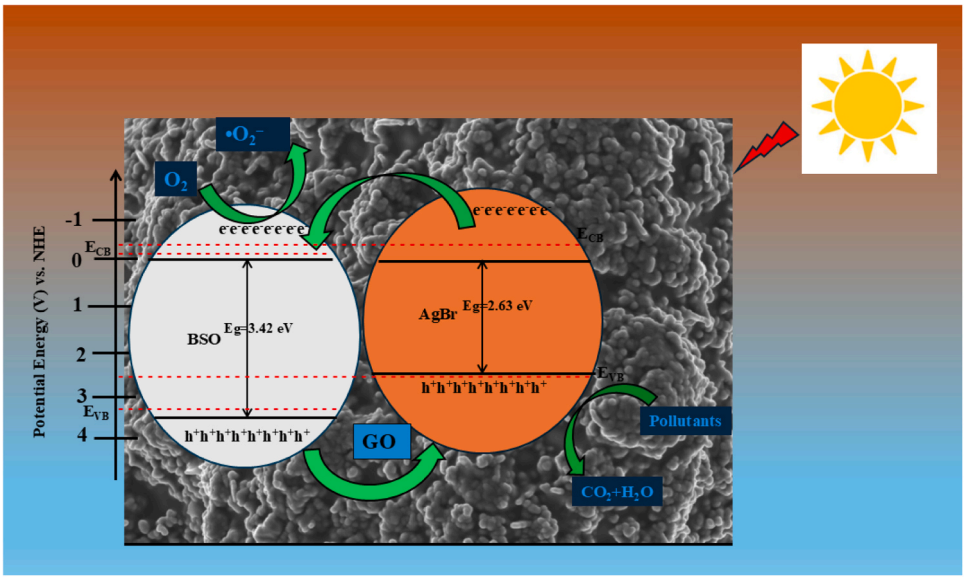

Fig. 17. A proposed photocatalytic mechanism for the degradation of TCN and RhB over GO/BSO/AgBr heterojunction photocatalyst.

4. Conclusion

In summary, a novel GO/BSO/AgBr photocatalyst was successfully prepared via the modification of Bi_2SiO_5 with GO and AgBr using the co-precipitation method. Under visible light irradiation, GO/BSO/AgBr photocatalyst heterojunction degradation rate on TCN and RhB reached 95.83 and 97.02 % in 60 and 30 min, respectively. It was observed that the photocatalytic performance of the BSO improved due to its functionalization by the AgBr nanoparticles due to its SPR properties and the electron sink properties of the GO. In addition, the light absorption range of GO/BSO/AgBr heterojunction photocatalyst increased when compared with BSO, BSO/AgBr, which led to the extension of light adsorption into the visible range, the reduction of the electron-hole recombination rate, coupled with an increase in its specific surface area, provides more active sites for photocatalytic degradation of TCN and RhB. TCN and RhB were more rapidly broken down into small molecules due to photogenerated electron-hole pairs' improved separation and transfer efficiency with the formation of h+ and $\bullet O^{2-}$ with intense oxidation. The stability of the photocatalyst composites was confirmed as the catalytic activity still reached 86.47 % after a 5-cycle treatment run, proving that the synthesized photocatalyst can serve as a promising material for environmental remediation.

Declaration of Competing Interest

The authors declare that they have no known competing financial interests or personal relationships that could have appeared to influence the work reported in this paper.

Data availability

Data will be made available on request.

References

[1] C. Thambiliyagodage, Efficient photocatalysis of carbon coupled TiO2 to degrade pollutants in wastewater–a review, Environ. Nanotechnol., Monit. Manag. 18 (2022) 100737.
[2] H.M. Samuel, M.M. M'Arimi, C. Achisa Mecha, Synthesis, characterization, and photocatalytic performance of ZnFe2O4-g-C3N4 composites for tetracycline removal from contaminated water, J. Nanotechnol. 2024 (1) (2024) 6687926.
[3] E.O. Omotola, et al., Occurrence, detection and ecotoxicity studies of selected pharmaceuticals in aqueous ecosystems-a systematic appraisal, Environ. Toxicol. Pharmacol. 91 (2022) 103831.
[4] O.C. Olatunde, et al., Design of S-scheme CuInS2/CeO2 heterojunction for enhanced photocatalytic degradation of pharmaceuticals in wastewater, Langmuir 41 (4) (2025) 2480–2491.
[5] P.J. Mafa, et al., Dual charge transfer mechanisms in intimately bonded S-scheme heterojunction photocatalyst with expeditious activity toward environmental remediation, Adv. Sustain. Syst. (2025) 2401070.
[6] Y. Zhang, et al., Insight in degradation of tetracycline in mariculture wastewater by ultraviolet/persulfate advanced oxidation process, Environ. Res. 212 (2022) 113324.
[7] Q. Li, et al., Robust degradation of tetracycline via peroxymonosulfate activation over peanut-like Co4N/NC composite: spatial confinement and heterojunction effects, Sep. Purif. Technol. (2024) 129589.
[8] D. Masekela, et al., Internal piezoelectric field produced by tri-component (FTO: Sb-ZnO/MoS2) thin film for enhanced photocatalytic degradation of organic pollutants and antibacterial activity, Mater. Today Commun. (2024) 108500.
[9] M. Ismail, et al., Pollution, toxicity and carcinogenicity of organic dyes and their catalytic bio-remediation, Curr. Pharm. Des. 25 (34) (2019) 3645–3663.
[10] T.L. Yusuf, et al., The application of photoelectrocatalysis in the degradation of rhodamine B in aqueous solutions: a review, RSC Adv. 12 (40) (2022) 26176–26191.
[11] Kant, R., *Textile dyeing industry an environmental hazard*. 2011.
[12] T.A. Khattab, M.S. Abdelrahman, M. Rehan, Textile dyeing industry: environmental impacts and remediation, Environ. Sci. Pollut. Res. 27 (4) (2020) 3803–3818.
[13] R. Al-Tohamy, et al., A critical review on the treatment of dye-containing wastewater: ecotoxicological and health concerns of textile dyes and possible remediation approaches for environmental safety, Ecotoxicol. Environ. Saf. 231 (2022) 113160.
[14] D. Masekela, et al., Advancements in piezo-photocatalysts for sustainable hydrogen generation and pollutant degradation: a comprehensive overview of piezo-photocatalysis, J. Water Process Eng. 71 (2025) 107172.
[15] S. Gao, et al., Photocatalytic degradation of tetracycline by g-C3N4/stilbite under visible light: mechanistic insights and degradation pathways, Mater. Res. Bull. (2024) 113008.
[16] W. Xiao, et al., Preparation and evaluation of an effective activated carbon from white sugar for the adsorption of rhodamine B dye, J. Clean. Prod. 253 (2020) 119989.
[17] S. Sachdeva, A. Kumar, Preparation of nanoporous composite carbon membrane for separation of rhodamine B dye, J. Membr. Sci. 329 (1-2) (2009) 2–10.
[18] M.S. Kothari, K.A. Shah, Electrochemical oxidation for decolorization of Rhodamine-B dye using mixed metal oxide electrode: modeling and optimization, Water Sci. Technol. 81 (4) (2020) 720–731.
[19] D. Meng, et al., Study on CuO/g–C3N4 S–Scheme heterojunction for enhanced visible-light-driven photocatalytic degradation of xanthate, Opt. Mater. 143 (2023) 114259.
[20] A.O. Oluwole, E.O. Omotola, O.S. Olatunji, Pharmaceuticals and personal care products in water and wastewater: a review of treatment processes and use of photocatalyst immobilized on functionalized carbon in AOP degradation, BMC Chem. 14 (2020) 1–29.
[21] S. Shafafi, et al., Impressive visible-light photocatalytic performance of TiO2 by integration with Bi2SiO5 nanoparticles: binary TiO2/Bi2SiO5 photocatalysts with nn heterojunction, Colloids Surf. A: Physicochem. Eng. Asp. 629 (2021) 127392.
[22] D. Liu, et al., Enhanced visible light photocatalytic performance of a novel heterostructured Bi4O5Br2/Bi24O31Br10/Bi2SiO5 photocatalyst, Appl. Catal. B: Environ. 172 (2015) 100–107.

[23] Y. Wu, et al., A facile Pechini method to synthesize novel Bi 12 SiO 20–Bi 2 SiO 5 heterostructure photocatalysts with enhanced visible light photocatalytic activity, J. Mater. Sci.: Mater. Electron. 29 (2018) 4503–4508.
[24] Y. Wu, et al., Preparation of Ag–Bi 12 SiO 20/Bi 2 SiO 5 with high visible light photocatalytic property: the synergistic effect of the heterojunction and the heterogeneous interface, J. Mater. Sci.: Mater. Electron. 32 (2021) 6976–6983.
[25] A.O. Oluwole, O.S. Olatunji, Enhanced photocatalytic degradation of naproxen in aqueous matrices using reduced graphene oxide (rGO) decorated binary BSO/g-C3N4 heterojunction nanocomposites, Chem. Eng. J. Adv. 12 (2022) 100417.
[26] J. Wang, et al., Novel three-dimensional flowerlike BiOBr/Bi2SiO5 p–n heterostructured nanocomposite for degradation of tetracycline: enhanced visible light photocatalytic activity and mechanism, ACS Sustain. Chem. Eng. 6 (11) (2018) 14221–14229.
[27] C.-T. Yang, et al., A novel heterojunction photocatalyst, Bi 2 SiO 5/gC 3 N 4: synthesis, characterization, photocatalytic activity, and mechanism, RSC Adv. 6 (47) (2016) 40664–40675.
[28] D. Liu, et al., Constructing a novel Bi2SiO5/BiPO4 heterostructure with extended light response range and enhanced photocatalytic performance, Appl. Catal. B: Environ. 236 (2018) 205–211.
[29] X.-J. Wen, et al., Photocatalytic degradation of ciprofloxacin by a novel Z-scheme CeO2–Ag/AgBr photocatalyst: influencing factors, possible degradation pathways, and mechanism insight, J. Catal. 358 (2018) 141–154.
[30] Y. Xie, et al., Synthesis and characterization of Bi2SiO5-coated Ag/AgBr photocatalyst with highly efficient decontamination of organic pollutants, Appl. Surf. Sci. 578 (2022) 152074.
[31] M.F.R. Samsudin, S. Sufian, Hybrid 2D/3D g-C3N4/BiVO4 photocatalyst decorated with RGO for boosted photoelectrocatalytic hydrogen production from natural lake water and photocatalytic degradation of antibiotics, J. Mol. Liq. 314 (2020) 113530.
[32] A.O. Oluwole, et al., Fabrication of BiVO 4/Ag 2 CrO 4 heterojunction composites modified with graphene oxide for enhanced photoelectrochemical and photocatalytic performance, RSC Adv. 14 (51) (2024) 38044–38058.
[33] E.O. Ichipi, S.M. Tichapondwa, E.M. Chirwa, Plasmonic effect and bandgap tailoring of Ag/Ag2S doped on ZnO nanocomposites for enhanced visible-light photocatalysis, Adv. Powder Technol. 33 (6) (2022) 103596.
[34] R.A. Senthil, et al., A facile synthesis of nano AgBr attached potato-like Ag2MoO4 composite as highly visible-light active photocatalyst for purification of industrial waste-water, Environ. Pollut. 269 (2021) 116034.
[35] J. Liu, et al., Construction of AgBr/Bi2SiO5 composite with Z-scheme structure and its visible light photocatalytic performance, J. Mater. Sci.: Mater. Electron. 34 (11) (2023) 976.
[36] J. Di, et al., Advanced photocatalytic performance of graphene-like BN modified BiOBr flower-like materials for the removal of pollutants and mechanism insight, Appl. Catal. B: Environ. 183 (2016) 254–262.
[37] X. Wang, et al., AgBr/(Sr0. 6Bi0. 305) 2Bi2O7 heterostructured composites: fabrication, characterization, and significantly enhanced photocatalytic activity, Catalysts 9 (5) (2019) 394.
[38] Y. Ren, et al., BiPO4/Ag3PO4/Bi2SiO5 heterojunction: controllable synthesis and its enhancement of visible light catalytic activity, J. Mater. Sci.: Mater. Electron. 34 (15) (2023) 1200.
[39] Y. Hou, et al., Construction of novel BiOCl/MoS2 nanocomposites with Z-scheme structure for enhanced photocatalytic activity, Mater. Lett. 218 (2018) 110–114.
[40] X. Rao, et al., Ag3PO4/g-C3N4 nanocomposites for photocatalytic degradating gas phase formaldehyde at continuous flow under 420 nm LED irradiation, Chemosphere 244 (2020) 125462.
[41] S. Sha, et al., Synthesis and visible-light photocatalytic degradation of Ag 3 PO 4/AgBr/hydroxyapatite ternary nanocomposites prepared from oyster shells, RSC Adv. 11 (26) (2021) 15598–15607.
[42] M. Shang, W. Wang, L. Zhang, Preparation of BiOBr lamellar structure with high photocatalytic activity by CTAB as Br source and template, J. Hazard. Mater. 167 (1-3) (2009) 803–809.
[43] J. Di, et al., Constructing carbon quantum dots/Bi2SiO5 ultrathin nanosheets with enhanced photocatalytic activity and mechanism investigation, Chem. Eng. J. 302 (2016) 334–343.
[44] X. Miao, et al., Fabrication of an all solid Z-scheme photocatalyst g-C3N4/GO/AgBr with enhanced visible light photocatalytic activity, Appl. Catal. A: Gen. 539 (2017) 104–113.
[45] A. Olufemi Oluwole, P. Khoza, O.S. Olatunji, Synthesis and characterization of g-C3N4 doped with activated carbon (AC) prepared from grape leaf litters for the photocatalytic degradation of enrofloxacin in aqueous systems, ChemistrySelect 7 (45) (2022) e202203601.
[46] B. Ma, et al., Fabrication of WO 2.72/RGO nano-composites for enhanced photocatalysis, RSC Adv. 7 (5) (2017) 2606–2614.
[47] Z.S. Liu, et al., BiPO4/BiOBr p–n junction photocatalysts: one-pot synthesis and dramatic visible light photocatalytic activity, Mater. Res. Bull. 63 (2015) 187–193.
[48] A.O. Oluwole, O.S. Olatunji, Photocatalytic degradation of tetracycline in aqueous systems under visible light irridiation using needle-like SnO 2 nanoparticles anchored on exfoliated gC 3 N 4, Environ. Sci. Eur. 34 (2022) 1–14.
[49] C. Liu, et al., Construction of NiTiO3/g-C3N4 heterojunction with preferable photocatalytic performance for tetracycline degradation, J. Solid State Chem. (2024) 124953.
[50] T.L. Yusuf, et al., Charge redistribution in Nise2/Mos2 n–n heterojunction towards the photoelectrocatalytic degradation of ciprofloxacin, ChemElectroChem 11 (16) (2024) e202400309.
[51] T.L. Yusuf, et al., Rational design of S-scheme Cd0. 5Zn0. 5S/CeO2 heterojunction for enhanced photooxidation of antibiotics and photoreduction of Cr (VI), Ceram. Int. (2024).
[52] A. Ishikawa, et al., Oxysulfide Sm2Ti2S2O5 as a stable photocatalyst for water oxidation and reduction under visible light irradiation (λ≤ 650 nm), J. Am. Chem. Soc. 124 (45) (2002) 13547–13553.
[53] C. Zou, et al., Flower-like Bi2SiO5/Bi4MoO9 heterostructures for enhanced photocatalytic degradation of ciprofloxacin, Nanotechnology 31 (34) (2020) 345604.
[54] A.O. Oluwole, O.S. Olatunji, Synthesis and characterization of binary bismuth tungstate-graphitic carbon nitride (BWO/g-C3N4) heterojunction nanocomposites for efficient photodegradation of ibuprofen in aqueous media, J. Water Process Eng. 54 (2023) 104045.
[55] M. Moztahida, et al., Reduced graphene oxide-loaded-magnetite: a Fenton-like heterogeneous catalyst for photocatalytic degradation of 2-methylisoborneol, Chem. Eng. J. 370 (2019) 855–865.
[56] U.A.A. Yasin, et al., Engineering the band structure of CuO via decoration with AgBr to enhance its photocatalytic degradation performance, J. Mater. Sci. 58 (17) (2023) 7333–7346.
[57] J. Lyu, et al., Removal of tetracycline by BiOBr microspheres with oxygen vacancies: Combination of adsorption and photocatalysis, J. Phys. Chem. Solids 129 (2019) 61–70.
[58] Z. Mengting, et al., 2D Graphene oxide (GO) doped pn type BiOI/Bi2WO6 as a novel composite for photodegradation of bisphenol A (BPA) in aqueous solutions under UV–vis irradiation, Mater. Sci. Eng.: C 108 (2020) 110420.
[59] S. Gao, et al., Photocatalytic degradation of tetracycline by g-C3N4/stilbite under visible light: Mechanistic insights and degradation pathways, Mater. Res. Bull. 180 (2024) 113008.
[60] M. Jodeyri, M. Haghighi, M. Shabani, Plasmon-assisted demolition of antibiotic using sono-photoreduction decoration of Ag on 2D C3N4 nanophotocatalyst enhanced with acid-treated clinoptilolite, Ultrason. Sonochem. 54 (2019) 220–232.
[61] C. Teng, et al., Synthesis of Ag2CO3/TiO2/SiC with pH stability and chloride ion boosted for efficient photodegrading tetracycline under visible light, Chem. Eng. J. 488 (2024) 150983.
[62] Y. Huang, et al., Fabrication of novel flower-like Co3O4/g-C3N4 heterojunction for tetracycline degradation under visible light irradiation, Mater. Lett. 311 (2022) 131538.
[63] M. Hu, W. Chen, J. Wang, Photocatalytic degradation of tetracycline by La-Fe Co-doped SrTiO3/TiO2 composites: performance and mechanism study, Water 16 (2) (2024) 210.
[64] Y. Zhang, et al., Synthesis and visible-light photocatalytic property of Ag/GO/g-C3N4 ternary composite, Mater. Sci. Eng.: B 221 (2017) 1–9.
[65] S. Chand, A. Mondal, g-C3N4/ZrO2 composite material: a pre-eminent visible light-mediated photocatalyst for rhodamine B degradation in the presence of natural sunlight, Ceram. Int. 49 (3) (2023) 5419–5430.
[66] K. Spilarewicz-Stanek, et al., Understanding the role of silver nanostructures and graphene oxide applied as surface modification of TiO2 in photocatalytic transformations of rhodamine B under UV and vis irradiation, Materials 13 (20) (2020) 4653.
[67] S. Asoubar, et al., Hexavalent chromium reduction and Rhodamine B degradation by visible-light-driven photocatalyst of stannum indium sulfide-samarium vanadate, npj Clean. Water 6 (1) (2023) 27.
[68] T. Bavani, et al., Fabrication of novel AgVO3/BiOI nanocomposite photocatalyst with photoelectrochemical activity towards the degradation of Rhodamine B under visible light irradiation, Environ. Res. 200 (2021) 111365.
[69] C. Wang, et al., Degradation and mineralization of bisphenol A by mesoporous Bi2WO6 under simulated solar light irradiation, Environ. Sci. Technol. 44 (17) (2010) 6843–6848.
[70] X.-X. Zhang, X.-J. Wang, Y.-Y. Niu, Photocatalytic degradation of tetracycline by supramolecular materials constructed with organic cations and silver iodide, Catalysts 12 (12) (2022) 1581.
[71] D. Carrales-Alvarado, et al., Effect of surface area and physical–chemical properties of graphite and graphene-based materials on their adsorption capacity towards metronidazole and trimethoprim antibiotics in aqueous solution, Chem. Eng. J. 402 (2020) 126155.
[72] W. Dai, et al., Efficient and stable photocatalytic degradation of tetracycline wastewater by 3D Polyaniline/Perylene diimide organic heterojunction under visible light irradiation, Chem. Eng. J. 397 (2020) 125476.
[73] M. Gao, et al., Photocatalytic removal of rhodamine B using a novel g-C3N4-organic solid waste biochar composite: Pathway, key factors, and mechanism, Opt. Mater. (2024) 116001.
[74] H. Zheng, et al., Fabrication of PVDF membrane loaded with ultra-thin g-C3N4/FeOCl nanomaterials and study on catalytic and antifouling properties, Sep. Purif. Technol. 331 (2024) 125641.
[75] Y. Yang, et al., Construction of iodine vacancy-rich BiOI/Ag@ AgI Z-scheme heterojunction photocatalysts for visible-light-driven tetracycline degradation: transformation pathways and mechanism insight, Chem. Eng. J. 349 (2018) 808–821.
[76] Z. Shen, et al., Degradation of atrazine by Bi2MoO6 activated peroxymonosulfate under visible light irradiation, J. Hazard. Mater. 400 (2020) 123187.
[77] H. Zhang, et al., P25-graphene composite as a high performance photocatalyst, ACS Nano 4 (1) (2010) 380–386.
[78] S.K. Sahu, et al., Investigation of photocatalytic and DNA interaction of novel heterostructured GO/Bi2O3/ZnO nanocomposite, Mater. Sci. Energy Technol. 5 (2022) 324–333.

[79] Y. Zhou, et al., Construction of 3D porous g-C3N4/AgBr/rGO composite for excellent visible light photocatalytic activity, Appl. Surf. Sci. 458 (2018) 586–596.
[80] X. Liu, et al., Magnetically separable quaternary g-C3N4/Fe3O4/AgBr/rGO nanocomposite for enhanced photocatalytic degradation of ofloxacin in water under visible light irradiation, J. Ind. Eng. Chem. (2024).
[81] J. Luo, et al., Built-in electric field mediated S-scheme high-quality charge separation in BiVO4/NiAl-LDH heterojunction for highly efficient photocatalytic degradation of antibiotics, J. Alloy. Compd. 1008 (2024) 176572.
[82] J. Luo, et al., Generating a captivating S-scheme CuBi2O4/CoV2O6 heterojunction with boosted charge spatial separation for efficiently removing tetracycline antibiotic from wastewater, J. Clean. Prod. 357 (2022) 131992.